# Hydrogen states in mixed-cation $CuIn_{(1-x)}Ga_xSe_2$ chalcopyrite alloys: a combined study by first-principles density-functional calculations and muon spin spectroscopy

A.G. Marinopoulos[a], R.C. Vilão[a], H.V. Alberto[a], E.F.M. Ribeiro[a], J.M. Gil[a], P.W. Mengyan[b], M.R. Goeks[b], M. Kauk-Kuusik[c] and J.S. Lord[d]

[a]CFisUC, Department of Physics, University of Coimbra, P-3004-516 Coimbra, Portugal; [b]Department of Physics, Northern Michigan University, Marquette, Michigan 49855, USA; [c]Department of Materials and Environmental Technology, Tallinn University of Technology, Ehitajate tee 5, 19086 Tallinn, Estonia; [d]ISIS Facility, Rutherford Appleton Laboratory, Chilton, Didcot, Oxon OX11 0QX, United Kingdom

**ARTICLE HISTORY**
Compiled July 29, 2021

**ABSTRACT**

First-principles calculations were performed jointly with muon-spin ($\mu$SR) spectroscopy experiments in order to examine the electrical activity of hydrogen in mixed-cation chalcopyrite $Cu(In_{1-x},Ga_x)Se_2$ (CIGS) alloys and other related compounds commonly used as absorbers in solar-cell technology. The study targeted the range of Ga concentrations most relevant in typical solar cells. By means of a hybrid-functional approach the charge-transition levels of hydrogen were determined and the evolution of the defect pinning level, E(+/–), was monitored as a function of the Ga content. The use of E(+/–) as a metric of the charge-neutrality level allowed the alignment of band structures, thus providing the band offsets between the $CuInSe_2$ compound and the CIGS alloys. The $\mu$SR measurements in both thin-film and bulk CIGS materials confirmed that the positively-charged state is the thermodynamically stable configuration of hydrogen for p-type conditions. The interpretation of the $\mu$SR data further addressed the existence of a metastable quasi-atomic neutral configuration that was resolved from the calculations and led to a formation model for muon implantation.

**KEYWORDS**
chalcopyrite solar cells; ab initio calculations; hydrogen; muon spectroscopy

## 1. Introduction

Hydrogen is a common impurity in semiconductors and even at trace quantities it can have a strong impact on the macroscopic electronic properties and electrical behavior of the host material [1–4]. The effects of hydrogen in Cu-based chalcopyrite compounds and related mixed-cation $Cu(In_{1-x},Ga_x)Se_2$ (CIGS) alloys employed as absorbers in solar cells have been well documented in a number of studies. Hydrogen implantation in single-crystal $CuInSe_2$ (CIS) was responsible for a conductivity type conversion in the near-surface regions from an initially $p$-type material to $n$-type [5]. Fermi-level pinning in CIGS-based heterojunction devices was attributed to hydrogen and other interfacial

CONTACT A.G. Marinopoulos. Email: marinop@uc.pt

defects, and led to a rollover of the open-circuit voltage limiting device efficiencies [6]. The introduction of hydrogen in CIS single crystals was also shown to improve the lattice structural stability by avoiding the formation of a radiation damage layer [7]. Experimental studies based on muon-spin rotation spectroscopy ($\mu$SR) in CIS also concluded that the muonium analogue of hydrogen (a lighter short-lived isotope) is a shallow donor [8, 9], with the largest percentage of implanted muons thermalising in the positively-charged, electronically diamagnetic state $Mu^+$.

The electrical activity of hydrogen in the ternary CIS and $CuGaSe_2$ (CGS) chalcopyrite compounds has been thoroughly studied in the past by first-principles approaches [6, 10, 11] based on density-functional theory [12, 13]. For CIS the most recent study by Varley and coworkers [6] made use of the HSE06 hybrid functional [14–16], a choice that enabled a trusted reproduction of the experimental electronic gap. The calculated defect formation energies suggested that interstitial hydrogen can be the source of $n$-type conductivity, with its E(+/–) charge-transition level (also known as pinning level) lying inside the conduction band. In contrast, hydrogen in CGS was predicted to be a charge-compensating defect with the E(+/–) level positioned well inside the gap [6, 10, 11]. The more recent results placed this level at about 0.5 eV below the conduction-band edge [6]. Furthermore, DFT-based calculations also showed that hydrogen forms stable defect complexes with the acceptor-like copper vacancies in both CIS and CGS compounds rendering these defects electrically inactive [10]. Thus, hydrogen will counteract the electrical conductivity originating from these vacancy defects and will passivate $p$-type $Cu(In,Ga)Se_2$.

All the aforementioned studies point out a need to equally understand the behavior of hydrogen in the mixed-cation $Cu(In_{1-x},Ga_x)Se_2$ (CIGS) alloys with moderate Ga content where neither experimental nor theoretical studies of its electrical activity exist. CIGS-based materials have gradually replaced the ternary CIS compound as absorbers in solar-cell photovoltaic devices. Partial replacement of In by Ga leads to an increase of the band gap of the absorber from the 1.05 eV magnitude of CIS [17] to values in a range from 1.2 to 1.3 eV for the CIGS absorbers with the higher efficiencies [18]. These materials usually possess a Ga content, $x$, defined by the atomic ratio [Ga]/([Ga]+[In]), from 0.20 to 0.30. In addition, it is also common to make use of thin-film CIGS absorbers which are Cu deficient and $x$ attains higher values, of about 0.40 [19, 20].

The aim in the present study has been to identify the lowest-energy configurations of interstitial hydrogen and its dominant charge states in CIGS alloys with typical Ga concentrations [21]. First-principles calculations were performed adopting two different computational schemes; first, a semilocal DFT functional [22] in order to sample exhaustively the configurational space of all possible hydrogen configurations in the chalcopyrite lattices. Secondly, the hybrid HSE06 functional [14–16] which was used to obtain the band gaps, band offsets and defect charge-transition levels as a function of the Ga content.

Additionally, the results of the theoretical calculations were used for the interpretation of new and existing $\mu$SR-spectroscopy results on thin-film and bulk CIGS, as well as on the ternary CIS and $CuInS_2$ chalcopyrite compounds, where the positive muon $\mu^+$ is used as a local probe [23, 24]. Depth profiles were also obtained by implanting slow muons in different depths of the samples [20, 25]. The amplitude of the diamagnetic fraction was used as a marker for such profiling and a formation model is presented.

## 2. Theoretical and experimental preliminaries

### *2.1. Theoretical background on the first-principles calculations*

The first-principles calculations were based on density-functional theory [12, 13] and the projected augmented-wave (PAW) method [26]. The ab-initio VASP code [27–30] was used for this purpose. The core-valence interaction in these calculations was represented by pseudopotentials. The following electronic configurations were assumed as the valence shells for the various elements: H($1s^1$), Cu ($3p^6$, $3d^{10}$, $4s^1$), In($4d^{10}$, $5s^1$, $5p^1$), Se($4s^2$, $4p^4$) and Ga($3d^{10}$, $4s^2$, $4p^1$). Exchange and correlation effects were described within the generalized-gradient approximation (GGA) by employing the semilocal PBE functional [22]. The crystalline wavefunctions were expanded in a plane-wave basis that was limited by a maximum kinetic-energy cutoff of 430 eV. A Γ-centered 3×3×2 **k**-point mesh was used for performing the integrations over the Brillouin-zone during the bulk-crystal optimizations on the chalcopyrite 16-atom tetragonal unit cells ($I\bar{4}2d$ crystal system). The DFT-based semilocal calculations were also supplemented with additional ones performed by means of the HSE06 hybrid functional [14–16]. This functional admixes a screened non-local Hartree-Fock exchange portion to the semilocal PBE exchange and is known to reproduce the experimental band gaps of both metallic and semiconducting solids with very good accuracy [14–16].

The randomly-mixed CIGS systems were generated by simulating the ideal disorder state of the CIS-CGS binary solid solution [31]. 64-atom supercells were employed for this purpose. These supercells are periodic in three dimensions and were constructed by a 2×2×1 repetition of the 16-atom tetragonal chalcopyrite CIS cell along the three orthogonal lattice vectors, **a**, **b** and **c**, respectively. Ga atoms were then introduced substitutionally at the sites of the cation sublattice. The aim was to leave the Wyckoff 4*a* site occupied by Cu atoms unaltered, and simulate a quasi-random occupation of the 4*b* site by the group-III atoms (Ga and In). Two different sets of CIGS supercells were constructed; the first set with a Ga fraction, $x$, of 0.1875, and the second with $x$ equal to 0.3750. The calculations of the hydrogen states were performed using these 64-atom supercells. A 2×2×2 Monkhorst-Pack **k**-point mesh was employed in these cases, with a total of four non-equivalent **k** points in the respective Brillouin zones.

The formation energies $E_{\rm form}[H^q]$ of all minimum-energy hydrogen configurations were determined for each of its charge states $q$ ($q$=–1, 0 or +1), as a function of the Fermi-level position $E_F$ in the theoretical gap, $E_{\rm g}$. These calculations were performed using the hybrid HSE06 functional. The corresponding expression for the defect energetics is as follows [32]:

$$E_{\rm form}[H^q] = E_{\rm tot}[H^q] - E_{\rm tot}[\text{bulk}] - \mu_H + qE_F \qquad (1)$$

where $E_{\rm tot}[H^q]$ is the total energy of the supercell with hydrogen in the charge state $q$ and $E_{\rm tot}$[bulk] the total energy of the bulk-crystal supercell. $\mu_H$ is the chemical potential of hydrogen and in the present study was taken as half the total energy of a hydrogen molecule at T = 0 K. This choice corresponds to hydrogen-rich conditions, whereby the defect supercell is assumed to be in equilibrium with hydrogen gas, $H_2$(g). The Fermi level, $E_F$, is conventionally referenced with respect to the energy of the valence-band maximum of the bulk supercell, $E_{\rm V}$. A correction was also added to the formation energies of the $q$=–1 and $q$=+1 hydrogen states in order to account for the electrostatic interactions of the defect with its periodically generated images. The

corresponding multipole correction due to Makov and Payne [33] was used. Taking a value of 12 for the average static dielectric constant of CIS [6], the magnitude of the correction was equal to 0.14 eV.

### *2.2. Experimental set-up and preliminaries*

Both new and existing experimental results via muon spin spectroscopy on thin-film and bulk CIGS, as well as on the related ternary chalcopyrite semiconductors $CuInSe_2$ and $CuInS_2$, will be discussed in the present work. Details about the previous experimental measurements and samples can be found in references [8], [9], [20], [34] and [35], as cited in the Figure captions that follow. We also include new muon spin spectroscopy measurements on bulk CIGS and the $CuInS_2$ compound, undertaken at the ISIS Muon and Neutron Facility in Chilton, UK. The Ga content of the CIGS sample corresponds to a value around 20%, typical of practical solar cells, matching also that of the lower Ga-content CIGS material studied by the first-principles calculations. More specifically, $Cu(In_{0.79}Ga_{0.21})_{1.09}Se_{2.1}$ polycrystalline samples grown at Tallinn University of Technology were measured in transverse geometry, using an applied magnetic field $B = 0.01$ T. $CuInS_2$ crystallites (as in Ref. [8]) were measured in longitudinal geometry at $T = 20$ K.

Figure 1 shows the time muon-spin rotation spectrum obtained for the CIGS sample at $T = 10$ K and with an applied magnetic field (in transverse geometry) $B = 10$ mT. The spectrum reveals an oscillation at the Larmor frequency ($\omega_L = 1.3921(2)$ MHz) consistent with the spin precession of $\mu^+$. A slight upward shift of the precession frequency is present reflecting the presence of a transient state, as noted in previous measurements in chalcopyrite semiconductors [20] and other systems [36]. The amplitude of the oscillation can be compared with that obtained with a calibration using silver, thus providing the fraction of muons stopping in the diamagnetic $\mu^+$-like configuration. A similar procedure was adopted for all samples and experimental geometries, as detailed in the corresponding references.

## 3. Results

### *3.1. Structural and electron-band parameters of the CIGS alloys*

HSE06 calculations were carried out initially in order to determine the optimum fractions of non-local exchange, $\alpha$ (in %), that would best represent the salient electron and structural properties of the ternary CIS and CGS compounds. The corresponding 16-atom tetragonal chalcopyrite unit cells were employed. Gradually varying $\alpha$ in increments of 0.5%, the adopted criterion was to reproduce as close as possible the experimental direct band gaps of these compounds. Reported values of $E_g$ from experiments are equal to 1.05 eV for CIS [17] and 1.68 eV for CGS [37]. Exchange fractions of 30.5% and 31.5% were found to provide the best match of the calculated band gaps with the experimental ones (see Table 1). Additional HSE06 calculations also provided the spin-orbit corrections for both CIS and CGS, since it is known that the spin-orbit interaction is important in chalcopyrite compounds by causing a split of the valence bands [38]. This split brings the uppermost valence states towards higher energies, thus narrowing the band gaps. The corresponding shift of the valence-band maximum at the $\Gamma$ point, $\Delta_{sov}$, calculated by the HSE06 functional is listed in Table 1 for both CIS and CGS compounds. These magnitudes are consistent with previous

**Table 1.** Theoretical (HSE06) lattice constants and electron-band parameters of the CIS and CGS ternary compounds. The corresponding results were obtained using the optimized exact exchange fractions, $\alpha$, of 30.5% and 31.5% for CIS and CGS, respectively. The experimental lattice constants [40] and band gaps [17, 37] for CIS and CGS are also listed.

| parameter | CIS | | CGS | |
|---|---|---|---|---|
| | HSE06 | exp. | HSE06 | exp. |
| $a$ (Å) | 5.804 | 5.784 | 5.628 | 5.614 |
| $c$ (Å) | 11.719 | 11.616 | 11.095 | 11.030 |
| $E_g$ (eV) | 1.045 | 1.05 | 1.695 | 1.68 |
| $\Delta_{sov}$ (eV) | 0.088 | – | 0.065 | – |

first principles calculations that treated spin-orbit effects in CIS and CGS compounds [6, 39]. The $\Delta_{sov}$ shifts were added as post-corrections in order to obtain the final HSE06-based band gaps.

Using the optimum exchange fractions $\alpha$ for CIS and CGS, subsequent energy minimizations were performed with the HSE06 functional to optimize the lattice parameters for the bulk-crystalline CIS and CGS tetragonal unit cells. The corresponding values are listed in Table 1. Additional calculations were also performed in order to determine the magnitude of the lattice parameters of the CIGS lattices as a function of the Ga content. This was achieved by introducing substitutionally a single Ga atom at one of the In sites of the 16-atom CIS cell, thus generating a CIGS stoichiometry with an atomic-fraction occupancy of Ga, $x$, equal to 0.25. This optimization resulted in a decrease of the chalcopyrite lattice parameters of the initial CIS compound (see Figure 2). It can be seen that both $a$ and $c$ parameters change linearly with the Ga fraction, $x$, a finding that reflects the validity of Vegard's rule for these random chalcopyrite alloys [41, 42]. The resulting linear-fit curve thus serves as a benchmark for assigning corresponding lattice parameters to the 64-atom CIGS supercells. For the CIGS alloy with $x$=0.1875 the $a$ and $c$ parameters are equal to 5.771 Å and 11.605 Å, whereas for the CIGS alloy with $x$=0.3750 the respective values are 5.738 Å and 11.487 Å (see Figure 2(a)).

Following the assignment of the macroscopic lattice parameters, the structural optimization of both CIGS supercells consisted of minimizing the total energies with respect to all atomic displacements after initially arranging for various trial substitutions by Ga atoms at In sites. The replacement of In by Ga is an isovalent cation substitution and was not found to lead to any atomic jumps during the energy minimization. However, there was considerable structural relaxation originating from the local strain when the smaller atom (Ga) replaces the larger one (In). The semilocal PBE functional was employed to sample in more detail the configurational space of Ga-to-In substitutions. The lowest-energy CIGS supercells for each Ga stoichiometry, $x$, were eventually taken as representative of the final CIGS structures to be optimized by the hybrid HSE06 functional. Examination of the final atomic configurations showed that the structural relaxation consisted of extensive changes in bond orientations and angles, whereas the bond lengths largely retained their corresponding values from the ternary compounds. This outcome is consistent with measurements by x-ray absorption fine-structure spectrocopy on CIGS materials as a function of composition [43], where it was also observed that bond-bending is energetically favoured over bond stretching. More specifically, the nearest-neighbor $d_{Cu-Se}$ and $d_{In-Se}$ distances were

found equal to 2.45 Å and 2.60 Å following the HSE06 optimization in the CIS compound. The corresponding distances in the CIGS alloys remained very similar, with a deviation of ± 0.03 Å from the CIS values. Finally, the $d_{\mathrm{Ga-Se}}$ distances in the two alloys are equal to 2.43 Å (to within 0.02 Å).

The band gaps of both CIGS alloys were also calculated using the HSE06 functional for the fully relaxed lowest-energy supercells. Values of 1.148 eV and 1.238 eV were obtained for the CIGS alloys with Ga fractions of $x$=0.1875 and $x$=0.3750, respectively. These gaps include spin-orbit corrections for the respective valence bands, $\Delta_{\mathrm{sov}}$. The same value of 0.085 eV for $\Delta_{\mathrm{sov}}$ that was determined for the 16-atom unit cell with a single Ga atom ($x$=0.25) was assigned to both alloys. The variation of the exact $E_{\mathrm{g}}$ results, plotted in Figure 2(b), with Ga content, confirms the experimentally observed band bowing for the CIGS chalcopyrite alloys [41]. In principle, the band gaps of such random multicomponent alloys follow a quadratic dependence upon the fraction, $x$, with the corresponding expression given as follows [41]:

$$E_{\mathrm{g}}(x) = (1-x)\ E_{\mathrm{g}}[CIS] + x\ E_{\mathrm{g}}[CGS] - bx(1-x) \tag{2}$$

where $b$ is the optical-bowing parameter. A quadratic fit of all calculated band gaps presented in Figure 2(b) led to the following expression for the dependence on the Ga content: $E_{\mathrm{g}}(x) = 1.049 + 0.445x + 0.201x^2$ (in eV). The obtained bowing parameter, 0.201 eV, is consistent with the experimental observations where values of $b$ from 0.15 to 0.24 eV were reported [41]. Previous calculations of band gaps of CIS-CGS alloys based on hybrid-functional and Monte-Carlo approaches led to a bowing parameter equal to 0.16 eV [31]. Other DFT-based calculations using a local-density functional also reported a value of $b$ equal to 0.21 eV [41].

### *3.2. Hydrogen configurations: structures, formation energies and pinning levels*

Hydrogen was initially placed at all possible high-symmetry positions in the host lattices. These comprise the interstitial tetrahedral and hexagonal sites, the bond-center (BC) sites of the various cation–Se bonds, and the Se-side antibonding ($\mathrm{AB_{Se}}$) positions of the In–Se and Cu–Se bonds. More general interstitial positions of lower symmetry were also tried. Structural optimization was then performed with the semilocal PBE functional by minimizing the total supercell energies with respect to all atomic displacements. To account for the structural disorder which is inherent in the CIGS supercells, an effort was made to sample at least two different configurations inside the supercells for each distinct structural type of hydrogen and calculate their energies by means of the semilocal PBE functional. The final results showed that all the non-equivalent configurations of each structural group (BC, $\mathrm{AB_{Se}}$ and interstitial) had a well defined energy range (to within 0.03 eV). The hybrid HSE06 functional was eventually employed to determine the formation energies of the final lowest-energy configurations of hydrogen for each of its distinct types, and for each of its charge states, $\mathrm{H^+}$, $\mathrm{H^0}$ and $\mathrm{H^-}$.

The formation energies of hydrogen in the CIS compound and the two mixed-cation CIGS alloys are shown in Figure 3 for hydrogen-rich conditions. The plot depicts the energies of the lowest-energy hydrogen configuration, for each charge state. The results are marked by the structural type that each charge state adopts. More specifically, hydrogen in its positively-charged state, $\mathrm{H^+}$, resides most favorably at the BC sites of

the Cu–Se bonds (see Figure 4(a)). In contrast, hydrogen in its negative and neutral states, $H^-$ and $H^0$, prefers the tetrahedral sites and the more general interstitial sites of the lattices, respectively (see Figure 4(b), (c) and Figure 5).

Hydrogen in its positively charged state, $H^+$, was found to form minimum-energy configurations with the hydrogen nucleus occupying positions near the bond-centered (BC) sites of all possible cation-anion bonds. These configurations entail rather strong displacements of the ions forming these bonds and in the final relaxed structures there is an asymmetry in the positions of the respective cations (Cu, In or Ga) and anions (Se) with respect to the hydrogen nucleus. In particular, hydrogen is located closer to the Se ions in these BC configurations; thus it does not occupy the ideal (bulk) BC sites in these bonds. The lowest-energy (ground-state) $H^+$ configurations in CIS and both configurations in CIS and both CIGS alloys correspond to hydrogen residing near the BC site of the Cu–Se bond. The energetics of these BC configurations are summarized in Figure 6, where it can be seen that the $BC_{Cu-Se}$ states are favored by about 0.5 eV, irrespective of the Ga content. In these cases, during structural relaxation the Cu and Se atoms are displaced from 0.40 to 0.60 Å from their ideal bulk sites that occupied in the pristine supercells. The final local environment of $H^+$ turned out to be very similar in all materials, with the H–Cu and H–Se distances equal to 1.80 ± 0.02 Å and 1.55 ± 0.02 Å, respectively (see Figure 4(a)).

In its negatively charged state, $H^-$, hydrogen occupied tetrahedrally-coordinated interstitial sites. In these configurations the hydrogen atom is surrounded by four cations (see Figure 4); two Cu ions and two group-III ions (In or Ga). The local environment, however, is strongly asymmetric with the hydrogen nucleus drawn much closer to the two group-III ions with distances in the range from 1.60 to 2.20 Å, whereas the two Cu ions are further away (beyond 2.60 Å). In contrast to the $H^+$ state, the energies of the different tetrahedral $H^-$ configurations lie within a very small energy interval (see Figure 6). The Ga content has also a small effect on the ground state of $H^-$: for CIS and the CIGS alloy with the lower Ga content ($x$=0.1875), it is an (In/In) pair which is closer to the H nucleus in the lowest-energy $H^-$ configuration (see Figure 4(b)). The corresponding H–In distances lie within a range from 1.90 to 2.05 Å. In contrast, in the CIGS alloy with the higher Ga content ($x$=0.3750) the closest cation pair to hydrogen is a mixed one: a Ga ion (at 1.65 Å) and an In ion at 2.30 Å (see Figure 4(c)).

Overall, the results of the formation energies shown in Figure 3 clearly show that in both CIGS alloys hydrogen is an amphoteric defect, with the pinning level, E(+/–), lying inside the respective band gaps. This means that hydrogen can be either donor or acceptor depending upon the position of the Fermi level. Effectively, hydrogen will counteract the prevailing conductivity in the CIGS materials; it is a charge-compensating defect. The E(+/–) level is displaced deeper inside the gaps with increasing Ga content. For the CIGS alloy with $x$=0.1875, the position of this level is at: $E(+/-) = E_C - 0.034$ eV, whereas for CIGS with $x$=0.3750 it is at: $E(+/-) = E_C - 0.118$ eV. In contrast, hydrogen in CIS is only thermodynamically stable in its positively-charged state, $H^+$, with the pinning level, E(+/–), positioned above the CB edge, $E_C$ (see Figure 3). thus, it is a shallow-donor defect, and will tend to drive CIS $n$-type. This agrees with the recent hybrid-functional calculations in CIS [6] and earlier analyses based on $\mu$SR spectroscopy for this compound [8, 9].

Another finding which characterizes all of the materials studied is that the neutral charge state of hydrogen, $H^0$, is not a thermodynamically stable state for any Fermi-level position in their gaps (see Figure 3). Such a behavior was also observed in previous studies in the ternary CIS and CGS compounds [6]. The present calculations

resolved several minimum-energy $H^0$ configurations which, however, possessed very high formation energies. All of the BC configurations were energy minima, in addition to the $AB_{Se}$ configuration of the In–Se bond. However, the lowest-energy (ground state) of neutral hydrogen was found to be an interstitial-type configuration, $H^0_{int}$, with hydrogen residing inside the empty interstitial space of the chalcopyrite lattice, irrespective of the Ga content (see Figure 5).

In these configurations the hydrogen is located very close to the tetrahedral interstitial site of the cation (Cu/In) sublattice, displaying a clear tendency towards mutual attraction with its nearest copper neighbor(s). Inspection of the energy landscape showed that the energy hypersurface for such interstitial configurations is considerably flat with the governing structural degree of freedom being the presence of one or two copper neighbors in the immediate vicinity of hydrogen. The corresponding H–Cu distances were recorded to be around 1.65 Å, whereas the rest of the atoms are at least 2.40 Å away from the hydrogen nucleus. The chief characteristic of these $H^0_{int}$ configurations in all three materials is that they are quasi-atomic; they retain a partial atomic character where the hydrogen atom keeps a considerable part of its $1s$ electron. More specifically, a sizeable percentage of the electron density is spherically symmetric ($1s$ type) and is centered at the hydrogen nucleus, despite the fact that there exists a significant delocalization of the unpaired electron (see Figure 5). This strong delocalization likely originates from the fact that $H^0_{int}$ polarises its surrounding environment. This leads to a spilling of the density of the hydrogen electron to the nearest copper atoms, but also to more distant selenium atoms as well (see Figure 5).

In order to examine quantitatively the degree of atomic character of the neutral hydrogen state calculations of the hyperfine tensor were performed [45]. In particular the isotropic part of the hyperfine constant (Fermi-contact term), $A_{iso}$, can serve as a measure of the electron-spin localization of the unpaired electron. The expression for the Fermi-contact term for neutral hydrogen is given by:[46]

$$A_{\text{iso}} = \frac{8\pi}{3}\, g_e \mu_e g_H \mu_H \rho_s(\mathbf{R}) \tag{3}$$

where: $g_e$ is the electron g-factor, $\mu_e$ the Bohr magneton, $g_H$ the hydrogen nuclear gyromagnetic ratio and $\mu_H$ its nuclear magneton. The spin density at the hydrogen-nucleus site, $\mathbf{R}$, is given by: $\rho_s = (\rho_\uparrow - \rho_\downarrow)$; namely, as the difference between the spin-up and spin-down electron densities. The isotropic constant was calculated by means of the hybrid HSE06 functional, with convergence calculations performed also with a higher kinetic-energy cutoff (550 eV). The resulting value was equal to 460 MHz ($\pm$ 10 MHz) for the $H^0_{int}$ configuration in the CIS compound [see Figure 5(a)]. This value corresponds to $\sim$ 32 % of the free-atom value of the hydrogen atom (1420 MHz) [47], verifying the presence of at least some partial atomic character in these neutral paramagnetic states. This value is also very similar to the isotropic hyperfine constants of muonium (after scaling for the respective nuclear magnetic moments) in other copper-based compounds, such as $Cu_2O$ and the cuprous halides where magnitudes in the range between 25 to 40% of the free-atom value were reported [48–50]. Interestingly, first-principles calculations of hydrogen states and their spin densities in $Cu_2O$ showed that interstitial hydrogen has a similar quasi-atomic character, with a significant delocalization of the electron-spin density to the nearest copper neighbors [51]. This finding is consistent with the present results in CIS and CIGS, lending also a plausible explanation for the existence of a moderate (not exceptionally high) value

**Table 2.** Band gaps and band offsets between the CIS compound and the CIGS alloys (in eV).

| | $E_g$ | VBO | CBO |
|---|---|---|---|
| CIS | 1.045 | – | – |
| CIGS ($x$=0.1875) | 1.148 | −0.014 | 0.089 |
| CIGS ($x$=0.3750) | 1.238 | −0.020 | 0.173 |

of the isotropic hyperfine constant for neutral hydrogen.

Despite the fact that the neutral charge state, $H^0$, is not a thermodynamically stable state in either CIS or the CIGS alloys (see Figure 3) it is still a minimum-energy metastable state that may be probed at conditions away from thermodynamic equilibrium. Our experimental measurements using muon-spin spectroscopy (where muons are implanted at high energies) reveal the formation of a neutral state in $CuInS_2$ with the characteristics discussed above, namely of a partial atomic character with a reasonably large value of the hyperfine interaction. These results will be discussed in subsections 3.4 and 3.5, where the metastable neutral configuration is shown to assume a most relevant role in the overall interpretation of the experimental data for both $CuInS_2$ and the CIGS materials.

### *3.3. Band alignment and offsets*

The determination of the hydrogen pinning level, E(+/–), as a function of Ga content presents also an opportunity to determine the band offsets of the CIGS materials with respect to the CIS ternary compound. Earlier studies have shown that the E(+/–) level is a very reliable charge-neutrality metric and can be used to line up the band structures of semiconductors [3]. The use of the E(+/–) level to align band structures presents important advantages over surface-based models which can display unwanted dependencies on interfacial dipoles [6].

The resulting band alignment between CIS and the CIGS alloys based on their respective E(+/–) levels is shown in Figure 7. The precice values of the valence-band (VBO) and conduction-band offsets (CBO) by taking as reference the CIS band positions are listed in Table 2. In agreement with existing photoemission measurements in CIGS thin films the calculated VBO's are nearly independent of the Ga content [52]. Clearly, the gradual increase of the band gap with increasing Ga content originates from the upward shift of the CIGS conduction bands with respect to the CB edge of CIS. This finding is also in agreement with experimental data [18] and earlier calculations of band offsets between the CIS and CGS ternary compounds [6, 53]. In those calculations the band alignment was based on the calculated ionization potentials of crystalline surface slabs, as well as on the respective hydrogen pinning levels, E(+/–), of the different crystalline compounds [6]. Bekaert and coworkers [53] further obtained band offsets of CIGS alloys with a variable Ga fraction, $x$, using the calculated branch-point energy. The corresponding CBO offset for $x$=0.25 was found equal to 0.14 eV. This value is numerically consistent with the present CBO results listed in Table 2, and falls within the expected range delimited by the two different CIGS systems studied here.

### *3.4. μSR experimental results*

Chalcopyrite semiconductors are $p$-type materials, thus the Fermi level is near the valence band and the thermodynamically stable state is diamagnetic $\mu^+$ (see subsection 3.2). The diamagnetic fraction is indeed the major component of the $\mu$SR signal in the deeper region of the CIGS film (see Figure 8) and at higher temperatures in the bulk samples (see Figure 9). However, a clear reduction of the diamagnetic fraction is seen near the surface in case of the CIGS film (see Figure 8) and at low temperatures in the case of bulk chalcopyrites (see Figure 9).

In order to confirm the presence of neutral muonium and characterize the fraction (of approximately 12%) of muon spin polarization which is not observed at low temperatures, an experiment in longitudinal geometry was performed at $T = 20$ K for the related $CuInS_2$ chalcopyrite compound (see Figure 10). The 12% missing fraction is seen to be gradually recovered with increasing (longitudinal) magnetic field; the observed fraction reaches about 95% (the maximum at $T = 300$ K) at $B \sim 0.2$ T.

The reduction of the diamagnetic fraction is related to the formation of atomic muonium as evidenced by the repolarization experiment (see Figure 10). The data in Figure 10 were therefore fitted to the usual isotropic repolarization curve [54], yielding a hyperfine parameter $A_{\mathrm{iso}} = 2.4(2)$ GHz. This value for the hyperfine interaction corresponds to $\sim 53$ % of the vacuum value (4463 MHz for the free muonium atom [4]). Such a magnitude inequivocally demonstrates the formation of a muonium state with a quasi-atomic character, similarly to the neutral interstitial hydrogen configuration described previously in the paper for CIS and CIGS (see Figure 5). The difference in the respective magnitudes of $A_{\mathrm{iso}}$ after rescaling by the ratio of the muon-to-proton magnetic moments ($\sim 3.18$) [4] should be traced to the different chemical composition (sulphur instead of selenium), the larger band gap of the $CuInS_2$ compound (1.55 eV) and smaller lattice parameters [55, 56]. Overall, the obtained $A_{\mathrm{iso}}$ values for the neutral hydrogen/muonium states in CIS and $CuInS_2$ are consistent with reported $A_{\mathrm{iso}}$ constants for normal muonium states in several elemental (Si, Ge) and compound semiconductors (InSb, GaAs) that reach as high as 70 % of the free-atom value [49]. Furthermore, from the systematic variation of the hyperfine interaction of muonium with band gap [49] the atomic character is more pronounced when the gap is larger. Thus a higher $A_{\mathrm{iso}}$ value is expected for $CuInS_2$.

In conclusion, the experiment shows that under certain conditions (low temperatures, surface region) the diamagnetic fraction decreases in favor of muonium formation. Similar results were obtained for the related quaternary semiconductor $Cu_2ZnSnS_4$ [20, 57]. The explanation for such a finding lies in the implantation process.

### *3.5. Final step in muon implantation*

We suggest the following process: the muon picks up an electron in the so-called charge exchange regime and arrives at the stopping site in the empty interstitial space of the chalcopyrite lattice in the neutral charge state. This configuration is similar to the interstitial configuration described in subsection 3.2 (see Figure 5) but without structural relaxation effects, such as the distortion of the surrounding ionic cage. Figure 11 depicts a configurational-coordinate diagram showing the minimum-energy neutral configurations obtained by the first-principles calculations for the CIGS alloy with the Ga fraction which matches more closely the one of the experimental samples. The transition from the incoming compact muonium to the diamagnetic (BC or $AB_{\mathrm{Se}}$)

muonium would normally proceed over a potential barrier, $E_b$ (see Figure 11). The height of this barrier will therefore determine the branching of the incoming muonium, namely the amount of muonium that can pass over the barrier and become diamagnetic or reflected back towards the paramagnetic (here missing) fraction with the partial atomic character [58, 59].

This now gives an explanation for the reduction of the diamagnetic fraction. i) In the surface region of the CIGS sample, the lattice is structurally distorted causing an increase of the barrier. The higher barrier in turn causes a larger muonium percentage to be reflected, thus the diamagnetic fraction gets smaller. ii) The energy barrier can be overcome through thermal excitation as temperature increases. However, at low temperatures thermal energy is small, thus a smaller muonium percentage makes it over the barrier and the diamagnetic fraction decreases.

## 4. Conclusions

The present study adopted a combined theoretical and experimental approach to examine the hydrogen states and their respective charge-transition levels in mixed-cation $Cu(In_{1-x},Ga_x)Se_2$ alloys with different Ga concentrations, $x$. The calculated $x$-dependent lattice parameters, band gaps and band offsets were consistent with existing experimental data.

In contrast to the CIS ternary compound, hydrogen in the CIGS alloys was found to be an amphoteric defect; even for the lower Ga-content CIGS alloy ($x$=0.1875) studied here the hydrogen pinning level, E(+/–), lies within the band gap. The E(+/–) level is displaced towards Fermi-level positions deeper in the gap with increasing Ga fraction. This tendency appears to be connected with the large conduction-band offsets that favor the stability of the negatively-charged hydrogen state.

For both the low and the high Ga-content CIGS alloys the positively-charged state, $H^+$, is the dominant charge state within the gap. In all minimum-energy $H^+$ configurations hydrogen invariably occupies all possible bond-centered (BC) sites in the chalcopyrite lattice; however, the BC sites of the Cu–Se bonds remain the energetically preferred sites for $H^+$, irrespective of the Ga content. In the negatively-charged $H^-$ states, instead, hydrogen occupies a multitude of distinct tetrahedral interstitial sites of the cation sublattice, with corresponding energies within a very small energy interval. The neutral paramagnetic $H^0$ state possesses a partial atomic character with a moderate isotropic hyperfine constant. It is also a high-energy defect, suggesting that it will probably remain inaccessible at conditions of thermodynamic equilibrium. Its presence, however, has important implications in situations characterized by a departure from thermodynamic equilibrium, and thus can play a relevant role for the interpretation of implantation experiments either with protons or muons.

The theoretical results are consistent with the experimental $\mu$SR data: here the main observed fraction for CIS, CIGS and $CuInS_2$ is a diamagnetic fraction assigned to the positively-charged state which is the thermodynamically stable state in these $p$-type materials. At low temperatures, the implantation of energetic muons also allowed access to a metastable neutral configuration with a reasonably high hyperfine interaction. This was assigned to the quasi-atomic interstitial configuration predicted by the first-principles calculations. A formation model is proposed for CIGS based on the present $\mu$SR results and the corresponding configurations determined from the calculations.

## Acknowledgements

The computer resources of the Department of Physics of the University of Coimbra were used, including the Navigator cluster at the Laboratory for Advanced Computing. ISIS muon beam time allocation from the Science and Technology Facilities Council, through experiment RB1920408 [60], and the support of the ISIS muon team are gratefully acknowledged.

## Funding

This work was supported with funds from FEDER (Programa Operacional Factores de Competitividade COMPETE) and from FCT-Fundação para a Ciência e Tecnologia (Portugal) under projects UID/FIS/04564/2016 and PTDC/FIS-MAC/29696/2017. The support by the European Regional Development Fund, Project TK141 is also gratefully acknowledged.

## References

[1] Ç. Kılıç and A. Zunger, *n-type doping of oxides by hydrogen*, Appl. Phys. Lett. 81 (2002), pp. 73–75.

[2] J. Robertson and P.W. Peacock, *Doping and hydrogen in wide gap oxides*, Thin Solid Films 445 (2003), pp. 155–160.

[3] C.G. Van de Walle and J. Neugebauer, *Universal alignment of hydrogen levels in semiconductors, insulators and solutions*, Nature 423 (2003), pp. 626–628.

[4] S.F.J. Cox, *Muonium as a model for interstitial hydrogen in the semiconducting and semimetallic elements*, Rep. Prog. Phys. 72 (2009), p. 116501.

[5] K. Otte, G. Lippold, H. Neumann, and A. Schindler, *Hydrogen in $CuInSe_2$*, J. Phys. Chem. Solids 64 (2003), pp. 1641–1647.

[6] J.B. Varley, V. Lordi, T. Ogitsu, A. Deangelis, K. Horsley, and N. Gaillard, *Assessing the role of hydrogen in Fermi-level pinning in chalcopyrite and kesterite solar absorbers from first-principles calculations*, J. Appl. Phys. 123 (2018), p. 161408.

[7] M.V. Yakushev, I.I. Ogorodnikov, V.A. Volkov, and A.V. Mudryi, *Incorporation of hydrogen in $CuInSe_2$: Improvements of the structure*, J. Vac. Sci. Technol. A 29 (2011), p. 051201.

[8] J.M. Gil, P.J. Mendes, L.P. Ferreira, H.V. Alberto, R.C. Vilão, N. Ayres de Campos, A. Weidinger, Y. Tomm, C. Niedermayer, M.V. Yakushev, R.D. Tomlinson, S.P. Cottrell, and S.F.J. Cox, *Modeling hydrogen in $CuInSe_2$ and $CuInS_2$ solar cell materials using implanted muons*, Phys. Rev. B 59 (1999), pp. 1912–1916.

[9] R.C. Vilão, H.V. Alberto, J.M. Gil, J.P. Piroto Duarte, N.A. de Campos, A. Weidinger, and M.V. Yakushev, *Hydrogen states in $CuInSe_2$ – a $\mu SR$ study*, Physica B 340-342 (2003), pp. 965–968.

[10] Ç. Kılıç and A. Zunger, *n-type doping and passivation of $CuInSe_2$ and $CuGaSe_2$ by hydrogen*, Phys. Rev. B 68 (2003), p. 075201.

[11] Ç. Kılıç and A. Zunger, *Doping of chalcopyrites by hydrogen*, Appl. Phys. Lett. 83 (2003), pp. 2007–2009.

[12] P. Hohenberg and W. Kohn, *Inhomogeneous electron gas*, Phys. Rev. 136 (1964), pp. B864–B871.

[13] W. Kohn and L.J. Sham, *Self-consistent equations including exchange and correlation effects*, Phys. Rev. 140 (1965), pp. A1133–A1138.

[14] J. Heyd and G.E. Scuseria, *Efficient hybrid density functional calculations in solids: As-*

*sessment of the Heyd-Scuseria-Ernzerhof screened Coulomb hybrid functional*, J. Chem. Phys. 121 (2004), pp. 1187–1192.

[15] J. Paier, M. Marsman, K. Hummer, G. Kresse, I.C. Gerber, and J.G. Angyan, *Screened hybrid density functionals applied to solids*, J. Chem. Phys. 124 (2006), p. 154709.

[16] M. Marsman, J. Paier, A. Stroppa, and G. Kresse, *Hybrid functionals applied to extended systems*, J. Phys.: Condens. Matter 20 (2008), p. 064201.

[17] M.V. Yakushev, F. Luckert, C. Faugeras, A.V. Karotki, A.V. Mudryi, and R.W. Martin, *Excited states of the free excitons in $CuInSe_2$ single crystals*, Appl. Phys. Lett. 97 (2010), p. 152110.

[18] R. Herberholz, V. Nadenau, U. Rühle, C. Köble, H.W. Schock, and B. Dimmler, *Prospects of wide-gap chalcopyrites for thin film photovoltaic modules*, Sol. Energy Mater. Sol. Cells 49 (1997), pp. 227–237.

[19] P.M.P. Salomé, J. Keller, T. Törndahl, J.P. Teixeira, N. Nicoara, R. Ribeiro Andrade, D.G. Stroppa, J.C. González, M. Edoff, J.P. Leitão, and S. Sadewasser, *CdS and $Zn_{1x}Sn_xO_y$ buffer layers for CIGS solar cells*, Sol. Energy Mater. Sol. Cells 159 (2017), pp. 272–281.

[20] H.V. Alberto, R.C. Vilão, R.B.L. Vieira, J.M. Gil, A. Weidinger, M.G. Sousa, J.P. Teixeira, A.F. da Cunha, J.P. Leitão, P.M.P. Salomé, P.A. Fernandes, T. Törndahl, T. Prokscha, A. Suter, and Z. Salman, *Slow-muon study of quaternary solar-cell materials: Single layers and p-n junctions*, Phys. Rev. Materials 2 (2018), p. 025402.

[21] B. Peace, J. Claypoole, N. Sun, D. Dwyer, M.D. Eisaman, P. Haldar, and H. Efstathiadis, *Characterization of $Cu(In,Ga)Se_2$ (CIGS) films with varying gallium ratios*, J. Alloys Compd. 657 (2016), pp. 873–877.

[22] J.P. Perdew, K. Burke, and M. Ernzerhof, *Generalized gradient approximation made simple*, Phys. Rev. Lett. 77 (1996), pp. 3865–3868.

[23] R.C. Vilão, J.M. Gil, A. Weidinger, H.V. Alberto, J. Piroto Duarte, N. Ayres de Campos, R.L. Lichti, K.H. Chow, and S.F.J. Cox, *Information on hydrogen states in II-VI semiconductor compounds from a study of their muonium analogues*, Nucl. Instrum. Methods Phys. Res., Sect. A 580 (2007), pp. 438–441.

[24] S.F.J. Cox, R.L. Lichti, J.S. Lord, E.A. Davis, R.C. Vilão, J.M. Gil, T.D. Veal, and Y.G. Celebi, *The first 25 years of semiconductor muonics at ISIS, modelling the electrical activity of hydrogen in inorganic semiconductors and high-$\kappa$ dielectrics*, Phys. Scr. 88 (2013), p. 068503.

[25] A.F.A. Simões, H.V. Alberto, R.C. Vilão, J.M. Gil, J.M.V. Cunha, M.A. Curado, P.M.P. Salomé, T. Prokscha, A. Suter, and Z. Salman, *Muon implantation experiments in films: Obtaining depth-resolved information*, Rev. Sci. Instrum. 91 (2020), p. 023906.

[26] P.E. Blöchl, *Projector augmented-wave method*, Phys. Rev. B 50 (1994), pp. 17953–17979.

[27] G. Kresse and J. Hafner, *Ab initio molecular dynamics for liquid metals*, Phys. Rev. B 47 (1993), pp. 558–561.

[28] G. Kresse and J. Hafner, *Ab initio molecular-dynamics simulation of the liquid-metal-amorphous-semiconductor transition in germanium*, Phys. Rev. B 49 (1994), pp. 14251–14269.

[29] G. Kresse and J. Furthmüller, *Efficient iterative schemes for ab initio total-energy calculations using a plane-wave basis set*, Phys. Rev. B 54 (1996), pp. 11169–11186.

[30] G. Kresse and D. Joubert, *From ultrasoft pseudopotentials to the projector augmented-wave method*, Phys. Rev. B 59 (1999), pp. 1758–1775.

[31] Y. Kumagai, Y. Soda, F. Oba, A. Seko, and I. Tanaka, *First-principles calculations of the phase diagrams and band gaps in $CuInSe_2$-$CuGaSe_2$ and $CuInSe_2$-$CuAlSe_2$ pseudobinary systems*, Phys. Rev. B 85 (2012), p. 033203.

[32] C. Freysoldt, B. Grabowski, T. Hickel, Jörg Neugebauer, G. Kresse, A. Zanotti, and C.G. Van de Walle, *First-principles calculations for point defects in solids*, Rev. Mod. Phys. 86 (2014), pp. 253–305.

[33] G. Makov and M.C. Payne, *Periodic boundary conditions in ab initio calculations*, Phys. Rev. B 51 (1995), pp. 4014–4022.

[34] J.M. Gil, H.V. Alberto, R.C. Vilão, J. Piroto Duarte, P.J. Mendes, N. Ayres de Campos, A. Weidinger, C. Niedermayer, M.V. Yakushev, R.D. Pilkington, R.D. Tomlinson, and S.F.J. Cox, *High-temperature trapping of muons in $CuInSe_2$ and $CuInS_2$*, Physica B 289–290 (2000), pp. 567–569.

[35] R.C. Vilão, J.M. Gil, H.V. Alberto, J. Piroto Duarte, N. Ayres de Campos, A. Weidinger, M.V. Yakushev, and S.F.J. Cox, *Muon diffusion and trapping in chalcopyrite semiconductors*, Physica B 326 (2003), pp. 181–184.

[36] R.C. Vilão, R.B.L. Vieira, H.V. Alberto, J.M. Gil, and A. Weidinger, *Role of the transition state in muon implantation*, Phys. Rev. B 96 (2017), p. 195205.

[37] J.L. Shay, B. Tell, H.M. Kasper, and L.M. Schiavone, *p-d Hybridization of the Valence Bands of I-III-$VI_2$ Compounds*, Phys. Rev. B 5 (1972), pp. 5003–5005

[38] J.L. Shay and H.M. Kasper, *Direct Observation of Cu d Levels in I-III-$VI_2$ Compounds*, Phys. Rev. Lett. 29 (1972), pp. 1162–1164.

[39] C. Persson, *Anisotropic hole-mass tensor of $CuIn_{1x}Ga_x(S,Se)_2$: Presence of free carriers narrows the energy gap*, Appl. Phys. Lett. 93 (2008), p. 072106.

[40] H.W. Spiess, U. Haeberlen, G. Brandt, A. Räuber, and J. Schneider, *Nuclear Magnetic Resonance in $I_B$–III–$VI_2$ Semiconductors*, Phys. Status Solidi (b) 62 (1974), pp. 183–192.

[41] S.H. Wei and A. Zunger, *Band offsets and optical bowings of chalcopyrites and Zn-based II-VI alloys*, J. Appl. Phys. 78 (1995), p. 3846.

[42] M.R. Balboul, H.W. Schock, S.A. Fayak, A.A. El-Aal, J.H. Werner, and A.A. Ramadan, *Correlation of structure parameters of absorber layer with efficiency of $Cu(In,Ga)Se_2$ solar cell*, Appl. Phys. A 92 (2008), pp. 557–563.

[43] C.S. Schnohr, H. Kämmer, C. Stephan, S. Schorr, T. Steinbach, and J. Rensberg, *Atomic-scale structure and band-gap bowing in $Cu(In,Ga)Se_2$*, Phys. Rev. B 85 (2012), p. 245204.

[44] K. Momma and F. Izumi, *VESTA3 for three-dimensional visualization of crystal, volumetric and morphology data*, J. Appl. Crystallogr. 44 (2011), pp. 1272–1276.

[45] K. Szász, T. Hornos, M. Marsman, and A. Gali, *Hyperfine coupling of point defects in semiconductors by hybrid density functional calculations: The role of core spin polarization*, Phys. Rev. B 88 (2013), p. 075202.

[46] J.M. Spaeth and H. Overhof, *Point Defects in Semiconductors and Insulators*, Springer Series in Materials Science Vol. 51, Springer-Verlag, Berlin Heidelberg, 2003.

[47] C.G. Van de Walle and P.E. Blöchl, *First-principles calculations of hyperfine parameters*, Phys. Rev. B 47 (1993), pp. 4244–4255.

[48] R.F. Kiefl, W. Odermatt, H. Baumeler, J. Felber, H. Keller, W. Kündig, P.F. Meier, B.D. Patterson, J.W. Schneider, K.W. Blazer, T.L. Estle, and C. Schwab, *Muonium centers in the cuprous halides*, Phys. Rev. B 34 (1986), pp. 1474–1484.

[49] S.F.J. Cox and C. Johnson, *The Systematics of Muonium Hyperfine Constants*, Hyperfine Interact. 158 (2004), pp. 255–260.

[50] S.F.J. Cox, J.S. Lord, S.P. Cottrell, J.M. Gil, H.V. Alberto, A. Keren, D. Prabhakaran, R. Scheuermann, and A. Stoykov, *Oxide muonics: I. Modelling the electrical activity of hydrogen in semiconducting oxides*, J. Phys.: Condens. Matter 18 (2006), pp. 1061–1078.

[51] D.O. Scanlon and G.W. Watson, *Uncovering the Complex Behavior of Hydrogen in $Cu_2O$*, Phys. Rev. Lett. 106 (2011), p. 186403.

[52] D. Schmid, M. Ruckh, and H.W. Schock, *Photoemission studies on $Cu(In,Ga)Se_2$ thin films and related binary selenides*, Appl. Surf. Sci. 103 (1996), pp. 409–429.

[53] J. Bekaert, R. Saniz, B. Partoens, and D. Lamoen, *Native point defects in $CuIn_{1-x}Ga_xSe_2$: hybrid density functional calculations predict the origin of p- and n-type conductivity*, Phys. Chem. Chem. Phys. 16 (2014), pp. 22299–22308.

[54] B.D. Patterson, *Muonium states in semiconductors*, Rev. Mod. Phys. 60 (1988), pp. 69–159.

[55] A.V. Mudryi, I.A. Victorov, V.F. Gremenok, A.I. Patuk, I.A. Shakin, and M.V. Yakushev, *Optical spectroscopy of chalcopyrite compounds $CuInS_2$, $CuInSe_2$ and their solid solutions*, Thin Solid Films 431–432 (2003), pp. 197–199.

[56] A. Shabaev, M.J. Mehl, and A.L. Efros, *Energy band structure of $CuInS_2$ and optical*

*spectra of $CuInS_2$ nanocrystals*, Phys. Rev. B 92 (2015), p. 035431.

[57] H.V. Alberto, R.C. Vilão, J.M. Gil, J. Piroto Duarte, R.B.L. Vieira, A. Weidinger, J.P. Leitão, A.F. da Cunha, M.G. Sousa, J.P. Teixeira, P.A. Fernandes, P.M.P. Salomé, K. Timmo, M. Loorits, A. Amato, H. Luetkens, T. Prokscha, A. Suter, and Z. Salman, *Muonium states in $Cu_2ZnSnS_4$ solar cell material*, J. Phys.: Conf. Series 551 (2014), p. 012045.

[58] E.L. da Silva, A.G. Marinopoulos, R.B.L. Vieira, R.C. Vilão, H.V. Alberto, J.M. Gil, R.L. Lichti, P.W. Mengyan, and B.B. Baker, *Electronic structure of interstitial hydrogen in lutetium oxide from DFT+U calculations and comparison study with $\mu$SR spectroscopy*, Phys. Rev. B 94 (2016), p. 014104.

[59] R.C. Vilão, R.B.L. Vieira, H.V. Alberto, J.M. Gil, A. Weidinger, R.L. Lichti, P.W. Mengyan, B.B. Baker, and J.S. Lord, *Barrier model in muon implantation and application to $Lu_2O_3$*, Phys. Rev. B 96 (2018) p. 115201.

[60] R.C. Vilão, J.S. Lord, H.V. Alberto, P.W. Mengyan, J.M. Gil, E. Ribeiro, and M.R. Goeks, *STFC ISIS Neutron and Muon Source*, 2020.

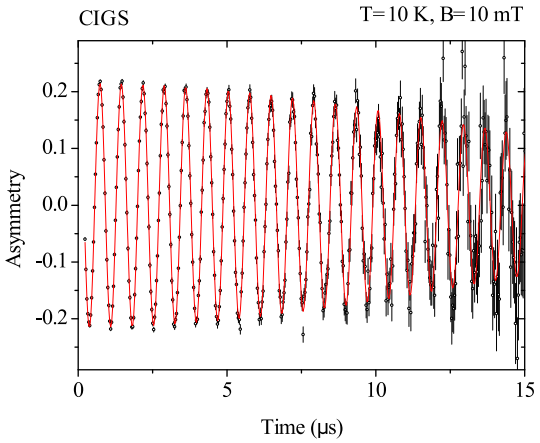


**Figure 1.** Muon-spin rotation asymmetry spectrum at $T = 10$ K and $B = 10$ mT of a polycrystalline sample of $Cu(In_{0.79}Ga_{0.21})_{1.09}Se_{2.1}$ (CIGS). Slightly damped oscillations are observed, characteristic of the spin precession of $\mu^+$ (diamagnetic fraction). The red line is a fit of a gaussian-damped oscillation [8].

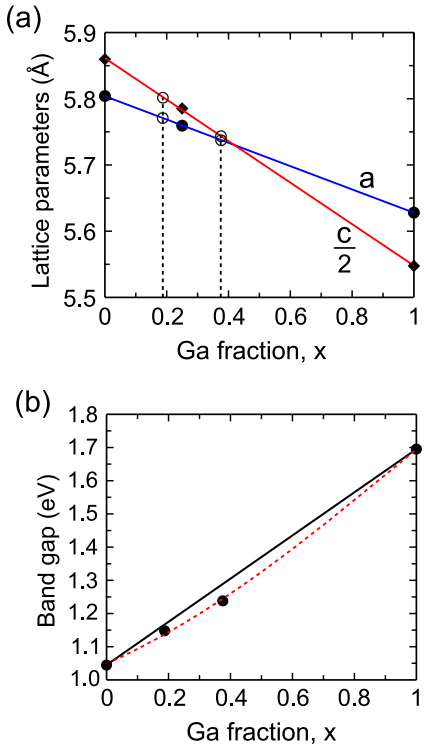


**Figure 2.** (a) Lattice parameters of the CIGS lattices as a function of Ga content. The filled symbols represent the results from the HSE06 optimizations using the 16-atom chalcopyrite unit cells. The open circles denote the parameters assigned to the CIGS supercells with $x$=0.1875 and $x$=0.3750. (b) Band gaps of CIGS materials as a function of Ga content. The filled circles represent the band gaps obtained by the HSE06 calculations for the ternary CIS and CGS compounds, and the CIGS supercells with $x$=0.1875 and $x$=0.3750. The dashed red curve is the result of the quadratic regression of the exact data (filled circles).

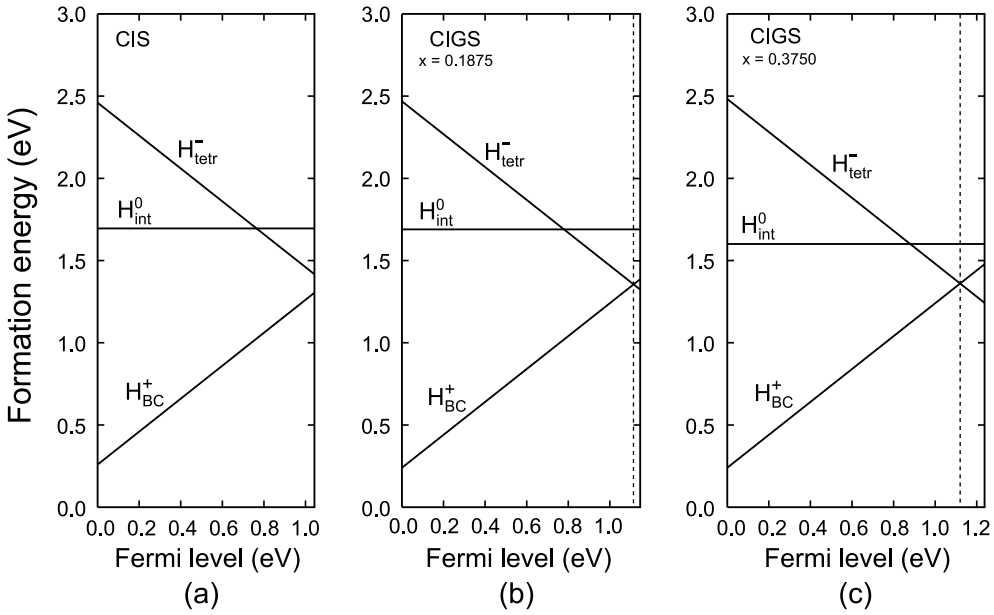


**Figure 3.** Formation energies of the hydrogen states in CIS and the two CIGS alloys as a function of the Fermi level in the respective band gaps. a) CIS compound. b) CIGS alloy with a Ga fraction of 0.1875. c) CIGS alloy with a Ga fraction of 0.3750. The dashed vertical lines denote the E(+/−) transition (pinning) levels. The results correspond to hydrogen-rich conditions and were obtained using the HSE06 functional. The reference value for the Fermi level is set at the valence-band maxima, $E_V$.

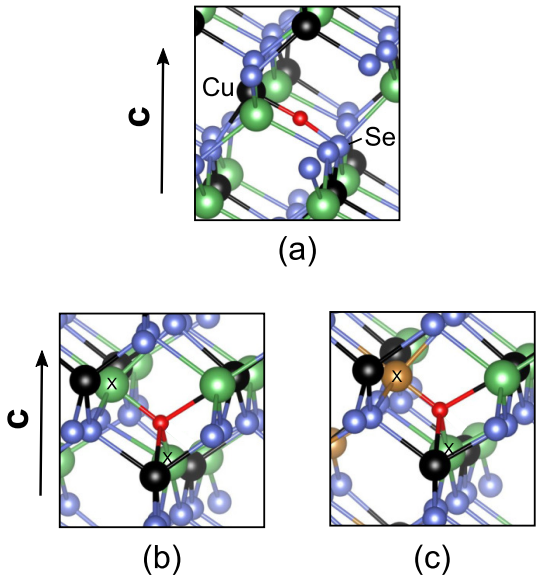


**Figure 4.** Atomistic structures of the lowest-energy positively- and negatively-charged hydrogen configurations. a) Structure of the $H^+$ state in CIS; hydrogen resides near the BC site of the Cu–Se bond. b) Structure of the $H^-$ state in the CIGS alloy with a Ga content of 0.1875. c) Structure of the $H^-$ state in the CIGS alloy with a Ga content of 0.3750. The various atoms are represented as follows: Indium as large green spheres, copper as black spheres, gallium as orange spheres, selenium as blue spheres and hydrogen as the small red sphere. The symbols $X$ denote the closer nearest-neighbor group-III (In and Ga) atoms to hydrogen (see text). The view is perpendicular to the chalcopyrite tetragonal **c** axis. The Figure was generated with the aid of the VESTA program [44].

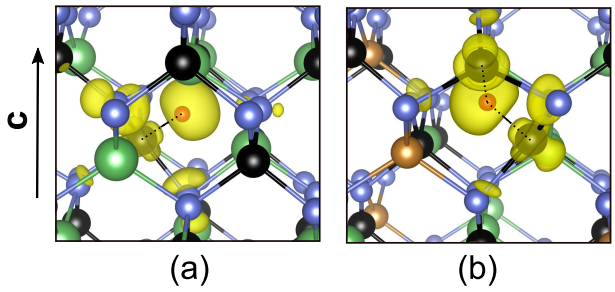


**Figure 5.** Atomistic structures and electron spin densities (in yellow) of the lowest-energy interstitial neutral states of hydrogen. (a) $H^0_{int}$ in CIS. (b) $H^0_{int}$ in CIGS with $x$=0.1875. The lines connect the hydrogen nucleus to its nearest copper neighbors (see text). The densities are shown for an iso-surface value of 0.002 $Å^{-3}$. The view is perpendicular to the chalcopyrite tetragonal **c** axis. The Figure was generated using the VESTA program [44].

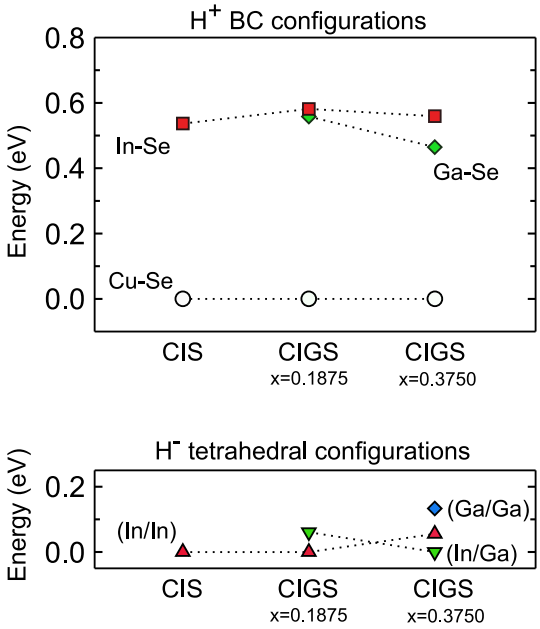


**Figure 6.** Relative energies of all minimum-energy $H^+_{BC}$ and $H^-_{tetr}$ configurations of hydrogen in the CIS compound and the two CIGS alloys. The structurally homologous configurations of the different materials are grouped together with lines connecting distinct symbols of the same colour. The lines are guide for the eye. The energy of the lowest-energy (ground state) configuration for each material defines the reference energy (set at zero). For the BC configurations the type of cation-anion is displayed. For the tetrahedral configurations the ions which are closer to hydrogen are denoted inside parentheses.

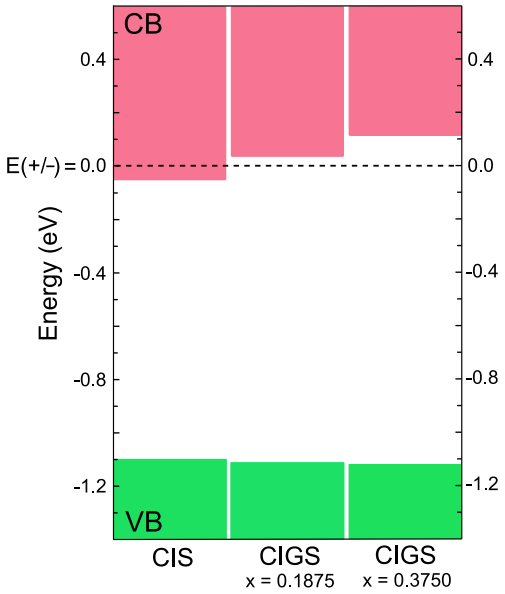


**Figure 7.** Alignment of the valence and conduction bands of the CIS compound and the CIGS alloys. The position of the hydrogen pinning level, E(+/−), sets the reference energy and is shown by the horizontal dashed line. The corresponding band offsets are listed in Table 2.

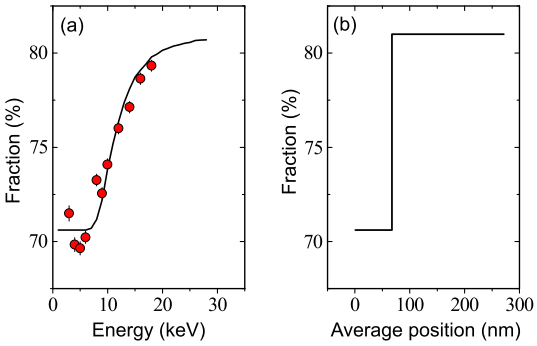


**Figure 8.** a) Diamagnetic fraction in the CIGS surface as a function of the implantation energy of positive muons (data for a temperature $T = 50$ K and an applied transverse magnetic field $B = 10$ mT, compiled from Ref. [20]). b) Unfolded reduction effect as a function of the average distance of the stopping muon from the surface of the CIGS sample, revealing the existence of two distinct regions (detailed in Ref. [20]).

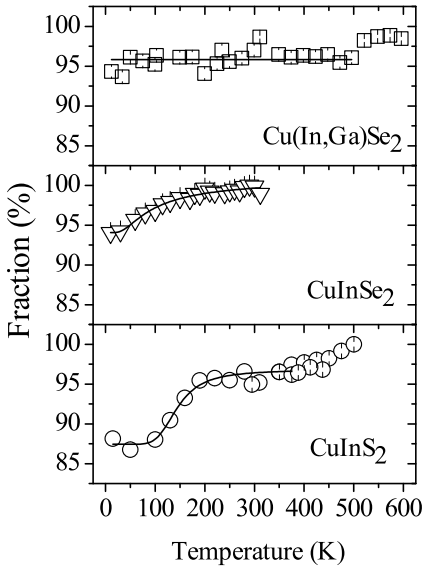


**Figure 9.** Diamagnetic fraction in CIGS, $CuInSe_2$ (from Ref. [9]) and $CuInS_2$ (from Ref. [35]), as a function of temperature. The lines are guide to the eye only.

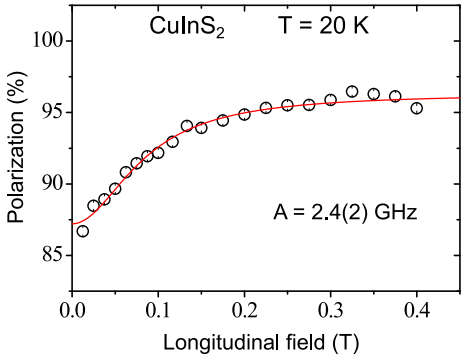


**Figure 10.** Repolarization curve for $CuInS_2$, at $T = 20$ K. The red line is a fit assuming an isotropic hyperfine interaction of $A = 2.4(2)$ GHz.

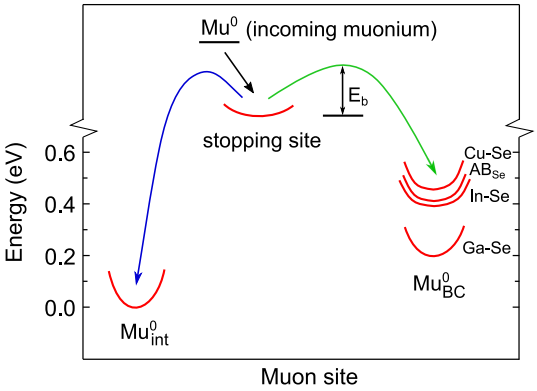


**Figure 11.** Schematic diagram of the reaction of atomic muonium with the host lattice. The energy minima (parabola in red lines) represent the calculated $H^0$ configurations at the interstitial, BC and $AB_{Se}$ sites obtained for the CIGS alloy with a Ga fraction of $x$=0.1875. The stopping site is depicted as the high-energy curve in the middle. The green trajectory at the right represents the formation of $Mu^0_{BC}$ (or $Mu^0_{AB_{Se}}$) and contributes to the *diamagnetic fraction*; the blue trajectory at the left represents the formation of $Mu^0_{int}$ and leads to the *missing fraction*.